

# Yttrium-doped NiMo-MoO<sub>2</sub> heterostructure electrocatalysts for hydrogen production from alkaline seawater

Received: 24 July 2024

Accepted: 31 December 2024

Published online: 17 January 2025

Check for updates

Shujie Liu<sup>1</sup>, Zhiguo Zhang<sup>1</sup>, Kamran Dastafkan<sup>2</sup>, Yan Shen<sup>1</sup>✉, Chuan Zhao<sup>2</sup>✉ & Mingkui Wang<sup>1</sup>✉

Active and stable electrocatalysts are essential for hydrogen production from alkaline water electrolysis. However, precisely controlling the interaction between electrocatalysts and reaction intermediates (H<sub>2</sub>O\*, H\*, and \*OH) remains challenging. Here, we demonstrate an yttrium-doped NiMo-MoO<sub>2</sub> heterogenous electrocatalyst that efficiently promotes water dissociation and accelerates the intermediate adsorption/desorption dynamics in alkaline electrolytes. Introducing yttrium into the NiMo/MoO<sub>2</sub> heterostructure induces lattice expansion and optimizes the *d*-band center of NiMo alloy component, enhancing water dissociation and H\* desorption. Yttrium doping also increases the concentration of oxygen vacancies in MoO<sub>2-x</sub>, which in turn accelerates the charge kinetics and the swift evacuation of \*OH intermediates from the active sites. Consequently, the Y-NiMo/MoO<sub>2-x</sub> heterostructure exhibits notable performance by requiring only 189 and 220 mV overpotentials to achieve current density of 2.0 A cm<sup>-2</sup> in alkaline water and seawater, respectively. This work provides a strategy to modulate heterostructure catalysts for scalable, economically viable hydrogen production from low-quality waters.

Water electrolysis is a promising process for harnessing renewable and sustainable energy sources and has emerged as a strategic pathway for the large-scale production and deployment of green hydrogen<sup>1,2</sup>. Among different water electrolysis technologies, alkaline water electrolysis has emerged as a leading technology for industrial-scale hydrogen production due to the simplicity of process design, relative technological maturity and low-cost operation<sup>3,4</sup>. Alkaline water electrolyzers (AWEs) provide a key advantage by reducing catalyst corrosion and enabling the use of non-noble metal catalysts for the hydrogen evolution reaction (HER), thereby advancing the economics of hydrogen production. However, AWEs have limitations in high current density and energy efficiency, which are critical for practical industrial-scale operation<sup>5</sup>. Recently, anion exchange membrane water electrolyzers have attracted greater attention due to their potential to overcome these limitations by offering higher ionic conductivity,

better energy efficiency, and the capability to operate at higher current densities (>500 mA cm<sup>-2</sup>)<sup>6,7</sup>. Nevertheless, under high current density conditions, the rapid consumption of electrolyte reactants coupled with the vigorous formation of a gas bubble layer on the electrodes surface remains a challenge to the activity and stability of the electrocatalysts<sup>8</sup>.

In alkaline media, HER kinetics is 2–3 orders of magnitude slower than in acidic media<sup>9,10</sup>. In addition to the adsorption free energy of H\* ( $\Delta G_{H^*}$ ), which serves as the primary activity descriptor for HER<sup>11</sup>, other steps including water dissociation<sup>12</sup> as well as factors such as the blocking effect caused by the adsorption of hydroxide ions (\*OH) onto active sites<sup>10</sup> become notably influential in alkaline conditions. According to the Sabatier principle<sup>13,14</sup>, single-component catalysts could be infeasible to simultaneously regulate water dissociation as well as the adsorption and desorption of H\* and \*OH species<sup>15</sup>. For this

<sup>1</sup>Wuhan National Laboratory for Optoelectronics, School of Optoelectronic Science and Engineering, Huazhong University of Science and Technology, Wuhan, PR China. <sup>2</sup>School of Chemistry, University of New South Wales, Sydney, Australia. ✉e-mail: [ciac\\_sheny@mail.hust.edu.cn](mailto:ciac_sheny@mail.hust.edu.cn); [chuan.zhao@unsw.edu.au](mailto:chuan.zhao@unsw.edu.au); [mingkui.wang@mail.hust.edu.cn](mailto:mingkui.wang@mail.hust.edu.cn)

reason, rational integration of active components with different roles is often required to form composite structures or alloy benchmark catalysts for alkaline HER<sup>16</sup>. In this case, NiMo alloy-based catalysts have proven to be highly promising due to the synergistic effect between Ni and Mo that effectively tunes the surface energetics, the strong hydrolysis dissociation ability of Ni, and the strong H<sub>2</sub> adsorption ability of Mo<sup>17–19</sup>. Accordingly, Zhang et al. reported a MoNi<sub>4</sub> electrocatalyst bolstered by MoO<sub>2</sub> cubic structures on nickel foam (NF) with a negligible onset potential for HER and an impressively low overpotential of merely 15 mV at a current density of 10 mA cm<sup>-2</sup><sup>20</sup>. However, the poor conductivity of MoO<sub>2</sub> would inevitably impede charge transfer between the NiMo alloy and the substrate at high current densities. On the other hand, optimizing the adsorption/desorption of HER intermediates over NiMo alloys and thereby enhancing the intrinsic activity under high current densities represents another challenge. Heteroatom doping introduces lattice strains due to size mismatch between dopant and host atoms, resulting in either tensile or compressive strains, which subsequently alter the electronic structure of the catalyst<sup>21,22</sup>. Doping of low-valent metals in metal oxide lattice structures has been previously demonstrated to modulate oxygen vacancy concentration with charge compensation effect<sup>23,24</sup>. Consequently, the doping strategy promises to effectively regulate the electronic structure of NiMo alloys and the oxygen vacancy concentration in MoO<sub>2</sub>, enabling the simultaneous optimization of the NiMo/MoO<sub>2</sub> heterostructure and consequently enhancing its HER performance in alkaline media.

Here, we introduce an yttrium-doped NiMo/MoO<sub>2</sub> heterostructure that synergistically modulates the *d*-band center of the NiMo alloy and oxygen vacancy defects in MoO<sub>2</sub> in one shot, realizing an enhanced HER activity and stability at high current densities. We found that doping with yttrium effectively facilitates the dissociation of water and H<sup>+</sup> adsorption-desorption on the NiMo surface, while oxygen vacancies in MoO<sub>2</sub> mediate \*OH and charge transfer. The developed Y-NiMo/MoO<sub>2-x</sub> electrocatalyst requires only 18 and 189 mV overpotential to yield current densities of 10 and 2000 mA cm<sup>-2</sup> in 1 M KOH and retains ca. 98.8% of the initial performance after 2500 h of continuous operation at a high current density of 1.0 A cm<sup>-2</sup>. The Y-NiMo/MoO<sub>2-x</sub> electrocatalyst also exhibit a low overpotential of 220 mV to achieve 2.0 A cm<sup>-2</sup> in natural alkaline seawater (1 M KOH + seawater). The fabricated yttrium-doped NiMo/MoO<sub>2-x</sub> electrocatalyst was applied to an anion exchange membrane (AEM) electrolyzer fed with natural alkaline seawater (3 M KOH + seawater) and achieved a high current density of 1.0 A cm<sup>-2</sup> at an ultralow cell voltage of 1.78 V, representing one of the best results among the noble metal-free catalysts<sup>25–27</sup>.

## Results

### Synthesis and characterizations of the Y-NiMo/MoO<sub>2-x</sub> electrocatalyst

The yttrium-doped NiMo/MoO<sub>2</sub> heterostructure electrocatalysts are fabricated with the aim of simultaneously modulating the electronic structure of the NiMo alloy and the oxygen vacancy concentration in MoO<sub>2</sub>. The yttrium-doped NiMoO<sub>4</sub> (denoted as Y-NiMoO<sub>4</sub>) was first grown on NF via a hydrothermal method and then transformed into the yttrium-doped NiMo/MoO<sub>2-x</sub> (denoted as Y-NiMo/MoO<sub>2-x</sub>) heterostructure catalysts via a reduction reaction (Supplementary Fig. 1)<sup>28</sup>. The impact of yttrium doping on the catalyst structure is evaluated by tuning the elemental Y:Ni mole ratios. Scanning electron microscopy (SEM) characterization shows Y-NiMoO<sub>4</sub> (Y:Ni mole ratio 2.0%) nanorods with smooth surface grown vertically on NF (Supplementary Fig. 2). No significant morphological changes were observed in the microscopic morphology of Y-NiMoO<sub>4</sub> compared to the pristine NiMoO<sub>4</sub>. After treatment at 500 °C in H<sub>2</sub>/Ar (V/V = 90/10) reduction atmosphere, the Y-NiMo/MoO<sub>2-x</sub> retained the nanorod morphology, but the surface became considerably rougher as shown in Fig. 1a.

Transmission electron microscopy (TEM) characterization shows black dots on the MoO<sub>2</sub> surface in Y-NiMo/MoO<sub>2-x</sub>, which can be ascribed to NiMo alloy nanoparticles (Fig. 1b). The lattice spacing of 2.44 Å and 2.08 Å correspond to the (200) and (121) planes of MoO<sub>2</sub> and NiMo components, respectively (Fig. 1c). Both lattice spacings are larger than those of NiMo/MoO<sub>2</sub> in the corresponding components (Supplementary Fig. 4b). In addition, NiMo/MoO<sub>2</sub> heterostructure depicts a faint diffuse halo in the SAED pattern after yttrium doping (Supplementary Fig. 5), indicating relatively weakened crystallinity. Similarly, a weak SEAD pattern is also observed for Y-NiMoO<sub>4</sub> compared to NiMoO<sub>4</sub> (Supplementary Fig. 6c and 6f). Energy dispersive spectroscopy (EDS) also shows a uniform distribution of the elements Ni, Mo, O and Y in the heterostructure (Supplementary Figs. 7 and 8).

The X-ray diffraction (XRD) pattern of NiMo/MoO<sub>2</sub> with and without yttrium doping depicts three main diffractions at 44.1°, 51.3°, 63.8°, and 75.6°, corresponding to (121), (310), (321), and (312) planes of NiMo alloy (Fig. 1d)<sup>29,30</sup>. The wide diffraction peak at 37.1° primarily corresponds to the (211) plane of MoO<sub>2</sub>, with possible contributions from the (200), (111), and (202) planes due to close lattice spacings<sup>31</sup>. The magnified XRD peaks in Fig. 1d reveal a shift to the lower-angle region with yttrium doping, indicating a gradual expansion of the corresponding lattice. This is because the ionic radius of Y (89 pm for Y<sup>3+</sup>) is larger than that of Ni (72 pm for Ni<sup>2+</sup>) and Mo (65 pm for Mo<sup>6+</sup>). Consistently, the lattice expansion can be observed by the XRD patterns of Y-NiMoO<sub>4</sub> with different Y:Ni mole ratios (0%, 1.0%, 2.0%, 4.0%, and 8.0%) (Supplementary Fig. 10). The diffraction peaks gradually become broader with increasing Y content and their intensity becomes weaker, suggesting that the introduction of Y leads to poor crystallinity, which is consistent with the TEM observation and is likely due to the increase in internal defects caused by the yttrium doping<sup>32</sup>. Raman spectroscopy further confirms the structural evolution of the heterostructure upon introducing yttrium. The characteristic peaks at 818.9, 893.1, and 940.1 cm<sup>-1</sup> correspond to Mo–O vibrations and show a slight blue shift after adding yttrium (Supplementary Fig. 11), which can be attributed to the lattice expansion<sup>33,34</sup>.

The electronic structure of NiMoO<sub>4</sub>, Y-NiMoO<sub>4</sub>, and Y-NiMo/MoO<sub>2-x</sub> is further studied by electron paramagnetic resonance (EPR) spectroscopy and X-ray photoelectron spectroscopy (XPS). The presence of oxygen vacancies (V<sub>O</sub>) is confirmed by the detected peak signal at *g* = 2.03 (Fig. 1e)<sup>35</sup>. The Y-NiMo/MoO<sub>2-x</sub> heterostructure shows the strongest EPR signal, indicating the increased oxygen vacancy concentration with yttrium doping and hydrogen annealing<sup>36</sup>. Fig. 1f shows high-resolution O 1s XPS spectra of NiMoO<sub>4</sub>, Y-NiMoO<sub>4</sub>, and Y-NiMo/MoO<sub>2-x</sub>, where the observed signals with binding energies of 530.3, 531.4, and 532.8 eV are assigned to lattice oxygen (O<sub>α</sub>), surface oxygen (O<sub>β</sub>), and the other weakly bound oxygen species (O<sub>γ</sub>), respectively<sup>37,38</sup>. Using the methods suggested by Jiang et al. to obtain deconvoluted peak areas, the oxygen vacancy content could be further estimated to be O<sub>β</sub>/(O<sub>α</sub>+O<sub>β</sub>+O<sub>γ</sub>)<sup>38</sup>. Consequently, the oxygen vacancy content in the Y-NiMoO<sub>4</sub> sample is ~11.3%, surpassing the value in NiMoO<sub>4</sub> (5.4%) (Supplementary Table 2). This indicates that the introduction of Y increases the concentration of V<sub>O</sub>. The V<sub>O</sub> concentration further increases up to 21.9% in the Y-NiMo/MoO<sub>2-x</sub> samples obtained by annealing Y-NiMoO<sub>4</sub> in a reduction atmosphere (H<sub>2</sub>/Ar). Therefore, the combination of yttrium doping with reduction proves to be an effective strategy to increase oxygen vacancy concentration<sup>39,40</sup>. Supplementary Fig. 14 summarizes the V<sub>O</sub> concentration assessed by different methods and the samples. It is obvious that the V<sub>O</sub> concentrations calculated from XPS and EPR follow the same trend, indicating that yttrium doping and hydrogen annealing are highly effective in producing V<sub>O</sub>. High-resolution XPS spectra of Ni 2*p* (Fig. 1g) and Mo 3*d* (Fig. 1h) of Y-NiMo/MoO<sub>2-x</sub> illustrate a shift towards higher binding energies with the addition of yttrium. The observed shift may also induce a downward shift of the *d*-band center of the NiMo alloy component<sup>41,42</sup>. The weaker peak

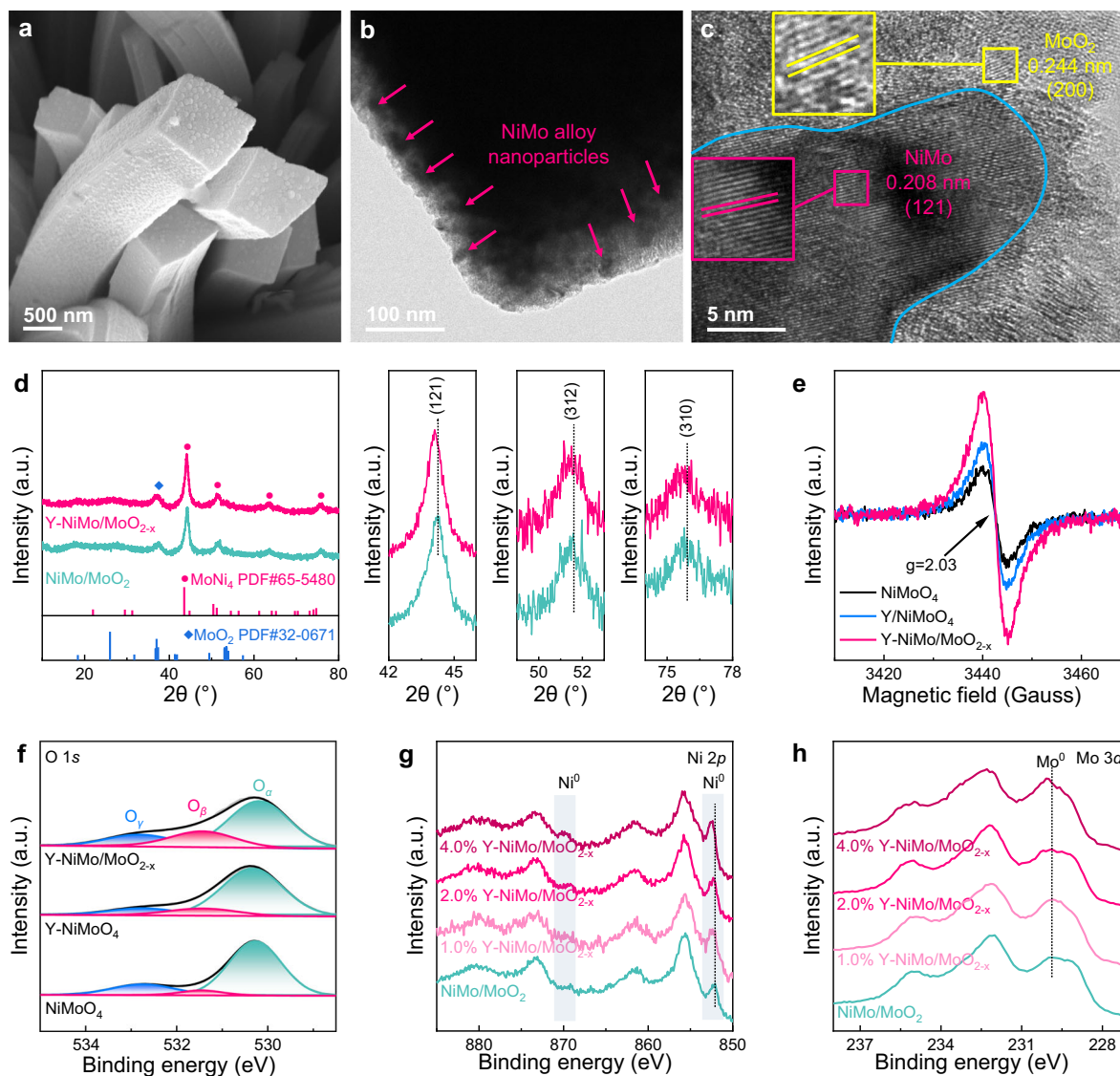


**Fig. 1 | Material characterization.** **a** SEM image of Y-NiMo/MoO<sub>2-x</sub> nanorod. **b** TEM image of Y-NiMo/MoO<sub>2-x</sub>. The positions of the NiMo alloy nanoparticles are marked using arrows. **c** HRTEM image of Y-NiMo/MoO<sub>2-x</sub>. The boundary between the NiMo alloy and MoO<sub>2</sub> phases is marked with a light blue line. **d** XRD patterns of NiMo/MoO<sub>2</sub> and Y-NiMo/MoO<sub>2-x</sub>. **e** EPR measurement of NiMoO<sub>4</sub>, Y-NiMoO<sub>4</sub>, and Y-NiMo/MoO<sub>2-x</sub>. High-resolution XPS of **f** O 1s, **g** Ni 2p, and **h** Mo 3d spectra for NiMo/MoO<sub>2</sub> doped with different ratios of Y (0%, 1.0%, 2.0%, and 4.0%).

intensity of the Y 3p XPS spectrum confirms a low yttrium content in the heterostructures (Supplementary Fig. 13b), in agreement with the TEM observation (Supplementary Fig. 8).

X-ray absorption spectroscopy was performed to further investigate the effects of yttrium-doping on the electronic structure and coordination environment of the NiMo/MoO<sub>2</sub> heterostructure. Figure 2a shows the X-ray absorption near-edge structure (XANES) spectra of Ni K-edge for NiMo/MoO<sub>2</sub> and Y-NiMo/MoO<sub>2-x</sub>. For comparison, Ni foil and NiO<sub>2</sub> references were measured in the same way. The pre-edge peaks of NiMo/MoO<sub>2</sub> and Y-NiMo/MoO<sub>2-x</sub> lie between those of the Ni foil and the NiO reference and show greater similarity to the Ni foil reference (Fig. 2a). The corresponding Fourier-transformed *k*<sup>3</sup>-weighted extended X-ray absorption fine structure spectra (EXAFS) show a dominant peak around -2.2 Å, which is attributed to the Ni-Mo (Ni) bond in the MoNi<sub>4</sub> alloy (Fig. 2b)<sup>43</sup>. Furthermore, when yttrium is introduced into the NiMo/MoO<sub>2</sub> system, the peak position of the Ni-Mo (Ni) bond shifts slightly to shorter bond lengths. This bond contraction suggests stronger Ni-Mo (Ni) interactions, which are expected to improve the stability of the catalyst<sup>44</sup>. The Mo K-edge

XANES spectra reveal that the pre-edges of NiMo/MoO<sub>2</sub> and Y-NiMo/MoO<sub>2-x</sub> are close to those of the Mo foil, although they are slightly shifted to higher energies due to the presence of the MoO<sub>2</sub> phase (Fig. 2c)<sup>45</sup>. Notably, after doping with yttrium, both Ni K-edge and Mo K-edge absorption spectra shift to lower energies compared to undoped NiMo/MoO<sub>2</sub>, indicating a reduction in the average oxidation states of Ni and Mo<sup>19</sup>. This decrease in oxidation states enhances the metallic character of the Y-NiMo/MoO<sub>2-x</sub> catalyst and enables faster electron transfer during catalytic processes. As shown in the Fourier-transformed *k*<sup>3</sup>-weighted EXAFS spectra at the Mo K-edge (Fig. 2d), the NiMo/MoO<sub>2</sub> heterostructure, both before and after yttrium doping, exhibits Mo-Ni bonds associated with the NiMo alloy phase and Mo-O bonds corresponding to the MoO<sub>2</sub> phase<sup>46</sup>. After doping with yttrium, a shortening of the bond length is again observed, which is consistent with the shortening of the Ni-Mo bond, further supporting the conclusion that doping with yttrium strengthens the bonding interactions and increases the structural stability of the catalyst. The XANES at Y K-edge indicates that the pre-edge peak of Y-NiMo/MoO<sub>2-x</sub> is situated between those of the Y foil and Y<sub>2</sub>O<sub>3</sub> (Supplementary Fig. 15),

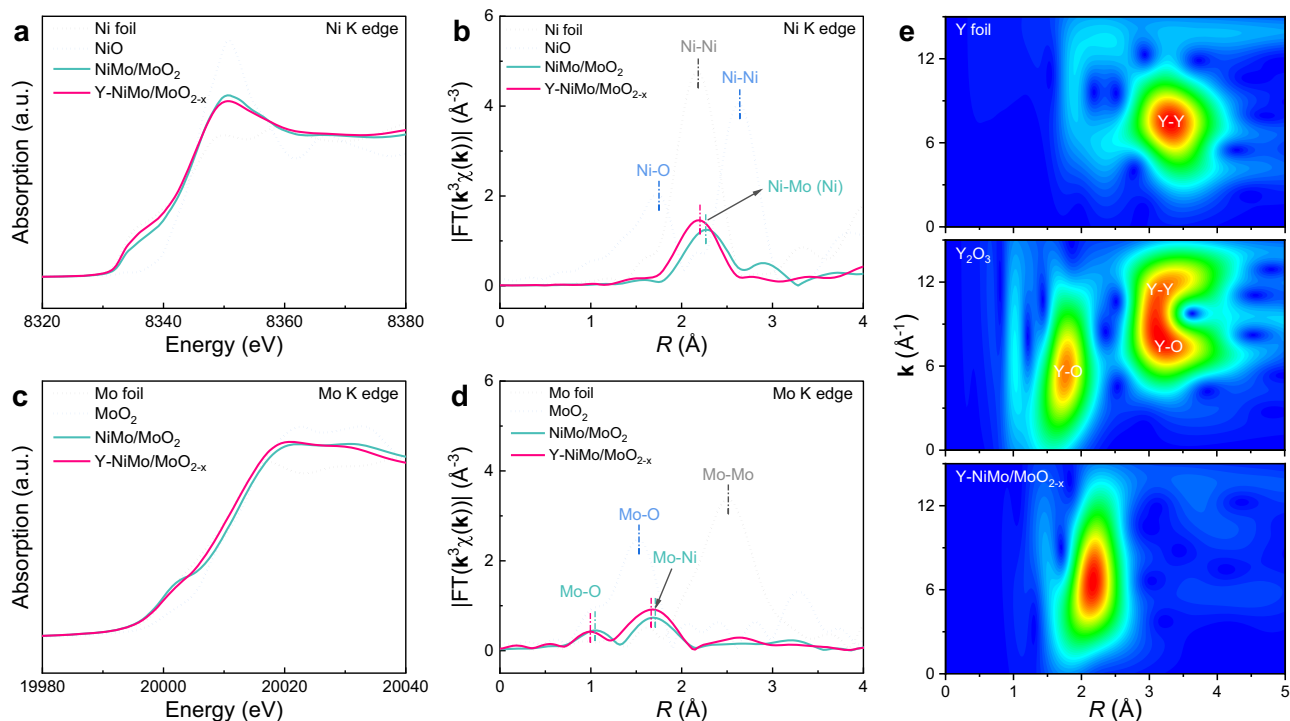


**Fig. 2 | Analysis of the electron structure and coordination environment.** The Ni K-edge (a) XANES and (b)  $k^3$ -weighted EXAFS spectra of Ni foil, NiO, NiMo/MoO<sub>2</sub> and Y-NiMo/MoO<sub>2-x</sub>.  $R$  represents the radial distance. The Mo K-edge (c) XANES and (d)  $k^3$ -weighted EXAFS spectra of Mo foil, MoO<sub>2</sub>, NiMo/MoO<sub>2</sub> and Y-NiMo/MoO<sub>2-x</sub>.  $k^3$ -weighted EXAFS wavelet transform plots of Y foil, Y<sub>2</sub>O<sub>3</sub>, and Y-NiMo/MoO<sub>2-x</sub>.  $R$  and  $k$  represent the radial distance and the wave vector, respectively.

indicating that the valence state of Y in Y-NiMo/MoO<sub>2-x</sub> lies between Y<sup>0</sup> and Y<sup>3+</sup><sup>47</sup>. Additionally, model-based EXAFS fitting was performed on Y foil, Y<sub>2</sub>O<sub>3</sub>, and Y-NiMo/MoO<sub>2-x</sub> (Supplementary Fig. 16 and Supplementary Table 4). In the  $R$ -space spectra of Y-NiMo/MoO<sub>2-x</sub>, the main peak at *ca.* 2.18 Å corresponds to the Y–Ni(Mo) bond, while the peak at *ca.* 1.6 Å is attributed to the Y–O bond. This indicates that yttrium atoms in Y-NiMo/MoO<sub>2-x</sub> coordinate with metal atoms in the NiMo alloy and oxygen atoms in MoO<sub>2</sub>. Figure 2e presents the high-resolution wavelet transform EXAFS in both  $R$ -space and  $k$ -space, with the main scattering at  $R = 2.18$  Å and  $k = 6.58$  Å<sup>-1</sup> corresponding to the Y–Ni(Mo) bond. Moreover, no scattering corresponding to Y–Y bonds ( $R = 3.34$  Å and  $k = 7.50$  Å<sup>-1</sup>) is observed, as seen in the Y foil. This absence confirms that yttrium atoms are uniformly dispersed within the NiMo/MoO<sub>2</sub> heterostructure without forming agglomerates.

### Electrocatalytic HER performance

The electrochemical performance for HER was evaluated in alkaline electrolytes (1 M KOH) using a three-electrode cell configuration with the prepared electrocatalysts on NF support, a Hg/HgO electrode, and a 3 mm diameter graphite rod as working electrode, reference electrode, and counter electrode, respectively. The influence of synthesis parameters including yttrium doping concentration, annealing temperature and time on Y-NiMo/MoO<sub>2-x</sub> as HER electrocatalyst is shown in Supplementary Fig. 18. The results indicate that the heterostructure with an yttrium doping ratio of 2.0% (treated at 500 °C for 30 min) is the most active for HER. Therefore, this heterostructure (noted as Y-NiMo/MoO<sub>2-x</sub>) was used for the discussion below without special statement. Figure 3a presents the polarization curves of as-prepared electrodes via linear sweep voltammetry at a scan rate of 5 mV s<sup>-1</sup> with 90%  $iR$  compensation<sup>48</sup>. The Y-NiMo/MoO<sub>2-x</sub> electrode exhibits very small overpotentials of 18 mV and 47 mV at current densities of 10 mA cm<sup>-2</sup> and 100 mA cm<sup>-2</sup>, respectively, which are 9 mV and 16 mV lower than the values obtained for the NiMo/MoO<sub>2</sub> electrode. This is clear evidence of the significant effect of yttrium doping in enhancing

HER activity. Notably, the Y-NiMo/MoO<sub>2-x</sub> electrode shows impressively low overpotentials of 129 mV and 189 mV to achieve high current densities of 1.0 A cm<sup>-2</sup> and 2.0 A cm<sup>-2</sup>, respectively. In contrast, the NiMo/MoO<sub>2</sub> electrode requires 83 mV and 141 mV larger applied potential to deliver the same current densities. The notable activity achieved at high current densities is primarily attributed to the nanorod morphology with rough surface grown on a three-dimensional (3D) nickel foam. This morphology not only increases the active surface area to accelerate the transport of electrons and reactants but also facilitates the rapid release of gas bubbles under high current loading, thereby enhancing the electrocatalytic performance<sup>49,50</sup>. In addition, the wetting properties of the catalyst surfaces play a crucial role in mass transport, especially at high current densities. Contact angle measurements were performed to assess the hydrophilicity of the NF, NiMo/MoO<sub>2</sub>, and Y-NiMo/MoO<sub>2-x</sub> electrodes. As shown in Supplementary Fig. 22, the NiMo/MoO<sub>2</sub> heterostructure exhibits notably increased hydrophilicity compared to the hydrophobic nature of the Ni foam substrate. With further yttrium doping, the Y-NiMo/MoO<sub>2-x</sub> catalyst shows almost instantaneous electrolyte absorption within 60 ms, indicating its exceptional mass transfer capabilities. Supplementary Table 5 compares the overpotentials obtained for Y-NiMo/MoO<sub>2-x</sub> and recent state-of-the-art electrocatalysts for alkaline HER at current densities of 500 and 1000 mA cm<sup>-2</sup><sup>51</sup>. Supplementary Table 6 compares the electrochemical performances of Y-NiMo/MoO<sub>2-x</sub> and recently developed alkaline HER electrocatalysts with various doping strategies. The Y-NiMo/MoO<sub>2-x</sub> electrode in this study delivers a high activity especially at high current densities in 1 M KOH electrolyte. The ratio of H<sub>2</sub> to O<sub>2</sub> products was detected to be about 2:1, close to the theoretical value, indicating a Faraday efficiency close to unity (Supplementary Fig. 23). The electrocatalytic kinetics and intrinsic HER activity are studied via the respective Tafel slopes acquired from the HER polarization curves (Fig. 3b). The Y-NiMo/MoO<sub>2-x</sub> electrode exhibits a small Tafel slope of 22.7 mV decade<sup>-1</sup>, lower than the 44.2 mV decade<sup>-1</sup>

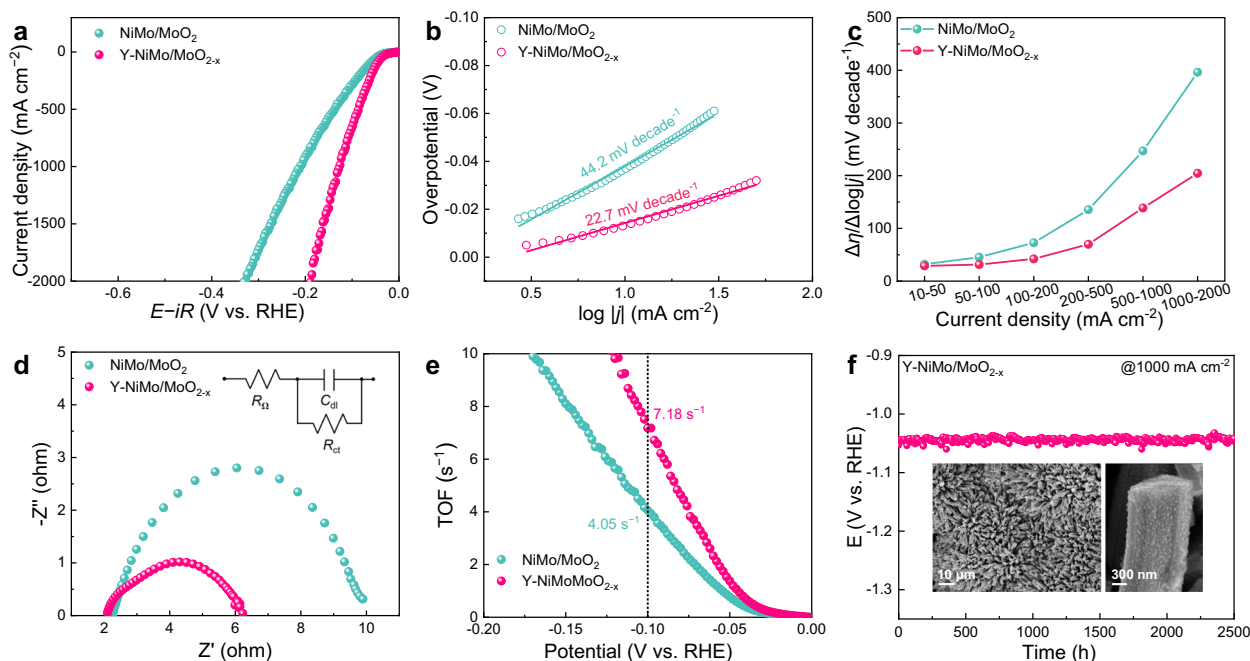


**Fig. 3 | Electrochemical characterization.** **a** Polarization curves of NiMo/MoO<sub>2</sub> and Y-NiMo/MoO<sub>2-x</sub> electrodes in 1 M KOH, **b** their corresponding Tafel plots, **c** the ratio of  $\Delta\eta/\Delta\log|j|$  at different current densities, **d** the Nyquist plots from electrochemical impedance spectroscopy measurements (inset shows the equivalent

circuit). **e** The calculated TOF curves. The black dotted line represents a potential of  $-0.1$  V vs. RHE. **f** The stability test of Y-NiMo/MoO<sub>2-x</sub> at 1000 mA cm<sup>-2</sup> in 1 M KOH. Inset shows SEM images of Y-NiMo/MoO<sub>2-x</sub> after durability test.

acquired for the NiMo/MoO<sub>2</sub> electrode. Consequently, the HER kinetics follows the Volmer–Tafel mechanism as a rate-determining step (RDS) over the surface of the Y-NiMo/MoO<sub>2-x</sub> electrode. In contrast, the RDS for the NiMo/MoO<sub>2</sub> electrode is separately attributed to the Heyrovsky pathway. This indicates that yttrium doping accelerates the HER reaction on NiMo/MoO<sub>2</sub> surface. To further evaluate the HER performance, the  $\Delta\eta/\Delta\log|j|$  ratio against current density is plotted for both electrodes to compare the overpotentials required as the current density increases in a broad range (Fig. 3c). With increasing the current density, the Y-NiMo/MoO<sub>2-x</sub> electrode maintains a small value of  $\Delta\eta/\Delta\log|j|$  ratio, whereas a marked increase can be observed for NiMo/MoO<sub>2</sub> electrode when the current density surpasses 500 mA cm<sup>-2</sup>. This verifies the higher electrocatalytic efficiency of the Y-NiMo/MoO<sub>2-x</sub> electrode at high current densities.

Electrochemical impedance spectroscopy (EIS) is further carried out to investigate the charge transfer at the electrode/electrolyte interface. Figure 3d compares the Nyquist plots of Y-NiMo/MoO<sub>2-x</sub> and NiMo/MoO<sub>2</sub> electrodes at  $-0.2$  V (*vs.* RHE). The Nyquist plots are fitted by a simple equivalent circuit (see inset), in which the resistance ( $R_{\Omega}$ ) symbolizes the internal resistance of electrolyte and electrode system, and the RC parallel circuit embodies the charge transfer across the electrode/electrolyte interface ( $R_{ct}$ ) and a corresponding double layer capacitance ( $C_{dl}$ ) to take interfacial characteristics into account<sup>5</sup>. The Y-NiMo/MoO<sub>2-x</sub> electrode shows a smaller  $R_{ct}$  (3.662  $\Omega$ ) than the NiMo/MoO<sub>2</sub> electrode (7.644  $\Omega$ ) in Supplementary Table 8. The turnover frequency (TOF) of the Y-NiMo/MoO<sub>2-x</sub> electrode is calculated to be 7.18 s<sup>-1</sup> at an overpotential of 100 mV, which is higher than that of 4.05 s<sup>-1</sup> for NiMo/MoO<sub>2</sub> (Fig. 3e). The incorporation of yttrium into the NiMo/MoO<sub>2</sub> heterostructure is shown to increase the electrochemical surface area (ECSA) from 9.9 to 11.3 cm<sup>2</sup> (Supplementary Fig. 26), indicating additional electrochemically active sites. The improvement in ECSA is attributed to the fact that yttrium dopants inhibit the agglomeration of NiMo/MoO<sub>2</sub> nanorod and promote a uniform and dense growth of the nanorods on the 3D NF substrate (Supplementary

Fig. 3). The long-term chronopotentiometry performed at a high current density of 1000 mA cm<sup>-2</sup> indicates a stable performance for 2500 h (Fig. 3f), demonstrating the robust stability of the Y-NiMo/MoO<sub>2-x</sub> electrode at high current density conditions and its suitability for practical applications. No obvious change in morphology is observed via the corresponding SEM images and the nano-rod structure tightly wrapped around the NF was maintained after the long-term stability test (inset in Fig. 3f). Additionally, compared to the NiMo catalyst, which showed a 55 mV increase in overpotential after 500 h of operation at 1 A cm<sup>-2</sup>, the Y-NiMo/MoO<sub>2-x</sub> catalyst exhibited only a 22 mV increase after 2500 h under the same conditions (Supplementary Fig. 27). This enhanced stability is primarily attributed to the uniform and dense growth of nanorods on the NF substrate after yttrium doping, which helps maintain structural integrity under the harsh conditions of high current density electrolysis. Further XPS analysis indicates that the decreased catalytic activity after prolonged stability testing is mainly due to the gradual oxidation of the surface NiMo alloy (Supplementary Fig. 28a, b)<sup>52</sup>. However, the increasing number of oxygen vacancies over time exposes additional active sites, potentially compensating for the degradation of the alloy sites and maintaining the long-term activity of the catalyst (Supplementary Fig. 28c)<sup>53</sup>.

### Insights into the underlying HER mechanism

Supplementary Fig. 29 presents the Nyquist and corresponding Bode plots of Y-NiMo/MoO<sub>2-x</sub> and NiMo/MoO<sub>2</sub> electrodes over a potential range of 0 to  $-1.0$  V (*vs.* RHE). Supplementary Tables 10 and 11 list the obtained parameters including the interfacial charge transfer resistance ( $R_{ct}$ ) and the corresponding double layer capacitance ( $C_{dl}$ ). Figure 4a indicates the variation of  $R_{ct}$  against the potential applied to the electrode. The obtained slope under polarization for the Y-NiMo/MoO<sub>2-x</sub> electrode is 28.6 mV decade<sup>-1</sup>, which is smaller than that of the NiMo/MoO<sub>2</sub> electrode (42.9 mV decade<sup>-1</sup>) and signifies the transition in HER kinetics from Volmer–Heyrovsky to Volmer–Tafel mechanism with

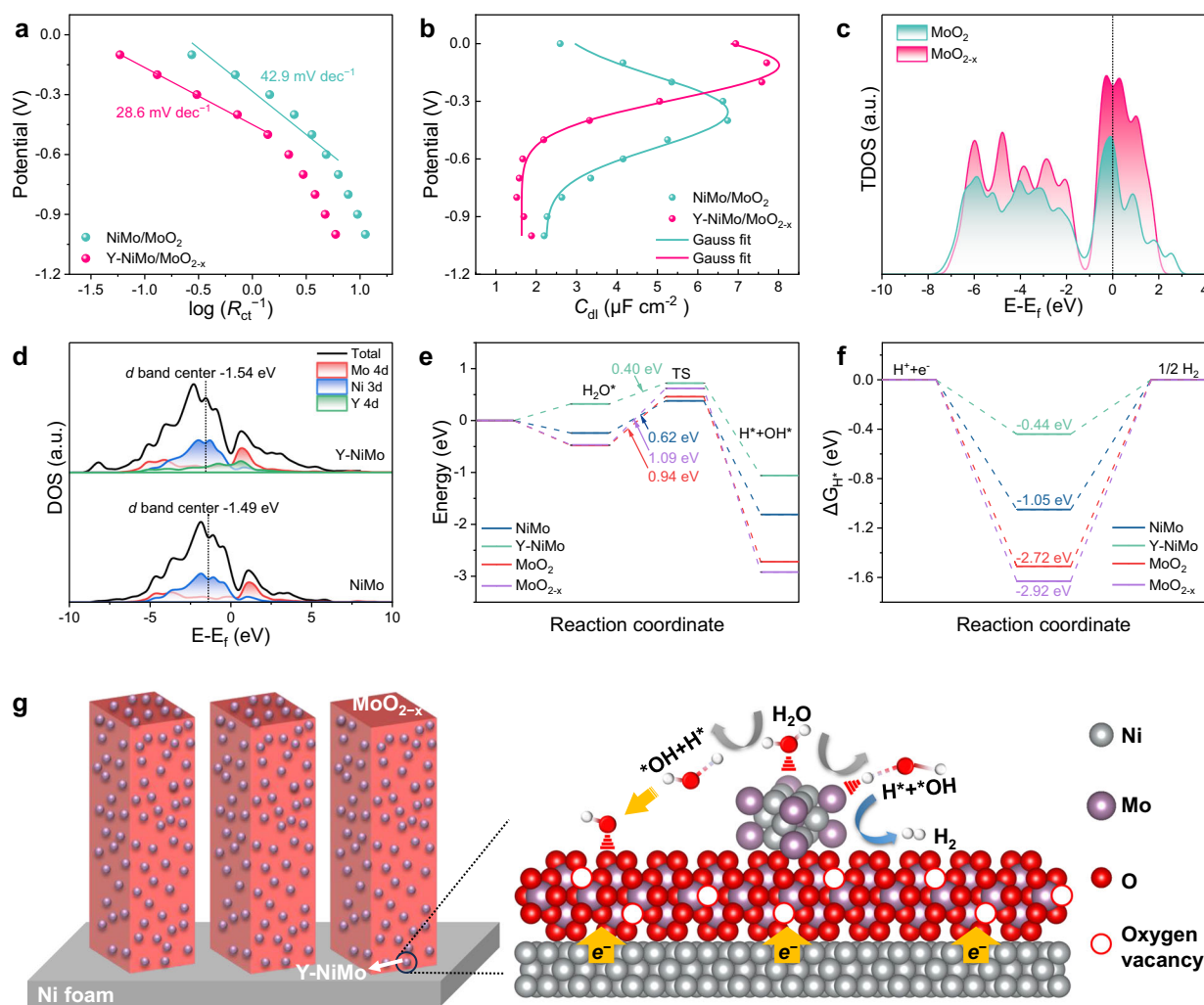


**Fig. 4 | The correlated calculation.** **a** The variation of  $\log(R_{ct}^{-1})$  with the applied potential onto electrode and **b** the obtained  $C_{dl}$  as a function of potential for NiMo/MoO<sub>2</sub> and Y-NiMo/MoO<sub>2-x</sub>. The charge transfer resistance  $R_{ct}$  and double layer capacitance  $C_{dl}$  are obtained from electrochemical impedance spectroscopy measurements. **c** The total density of states (TDOS) plots of MoO<sub>2</sub> and MoO<sub>2-x</sub> and **d** the

calculated projection density of states for NiMo and Y-NiMo from DFT calculation. **e** The illustration of free energies diagram of Volmer step and **f** the free energies diagram of H\* adsorption of Y-NiMo/MoO<sub>2-x</sub> as an efficient catalyst for the electrolysis of water in alkaline media. **g** Schematic diagram of the electrolysis of water in alkaline media.

yttrium doping of NiMo/MoO<sub>2</sub> heterostructure<sup>54</sup>. This observation agrees well with the RDS determined from the polarization curves (Fig. 4b). The effect of yttrium doping on the adsorption and desorption of the reaction intermediates (e.g., H<sub>2</sub>O\*, H\* and \*OH) on the surface of NiMo/MoO<sub>2</sub> is further analyzed using the double layer capacitance obtained from EIS measurements<sup>55</sup>. Fig. 4b shows the variation of  $C_{dl}$  against the applied potential on the NiMo/MoO<sub>2</sub> and Y-NiMo/MoO<sub>2-x</sub> electrodes. The  $C_{dl}$  values present a characteristic Gaussian distribution for both electrodes, suggesting a transition between occupied and unoccupied pseudo-capacitance on the electrode surface<sup>56</sup>. The Y-NiMo/MoO<sub>2-x</sub> electrode shows a peak in  $C_{dl}$  at a lower potential (-0.11 V) compared with the NiMo/MoO<sub>2</sub> electrode (-0.36 V). This verifies the facilitated water adsorption and the formation of HER intermediates over the Y-NiMo/MoO<sub>2-x</sub> electrode at low driving potentials, confirming the accelerated reaction kinetics<sup>55</sup>.

The electronic density of states (DOS) for the fabricated heterostructures is calculated via density functional theory (DFT) to gain a deeper insight into the origin of electron state modulation and intermediate binding energy tuning by yttrium doping and oxygen vacancies. Supplementary Fig. 31 presents the computational models, which encompass the (121) plane of NiMo alloy with and without yttrium

doping, along with the ( $\bar{1}11$ ) plane of MoO<sub>2</sub> featuring the presence and absence of oxygen vacancies. Figure 4c and Supplementary Fig. 32 present the calculated DOS for MoO<sub>2</sub> and MoO<sub>2-x</sub>. The abundance of oxygen vacancies is indicated by a heightened occupied state density in the vicinity of the Fermi level with respect to the pristine MoO<sub>2</sub>. Accordingly, the augmented conductivity of oxygen-vacancy-rich MoO<sub>2-x</sub> facilitates charge transfer during the HER<sup>57,58</sup>. Fig. 4d presents the partial density of states for NiMo and Y-NiMo alloys. All structural models exhibit metallic character with zero band gaps, indicating high electrical conductivity. The interaction between the adsorbent and the metal catalyst is elucidated by the *d*-band center model. The *d*-band center ( $\epsilon_d$ ) was calculated by the following equation:  $\epsilon_d = \frac{\int_{-\infty}^{\infty} \epsilon n_d(\epsilon) d\epsilon}{\int_{-\infty}^{\infty} n_d(\epsilon) d\epsilon}$ , where  $\epsilon$  is energy, and  $n_d(\epsilon)$  is the DOS<sup>59</sup>.

The *d*-band center shifts negatively from -1.49 to -1.54 eV upon the introduction of yttrium. Additionally, ultraviolet photoelectron spectroscopy (UPS) provides direct evidence for this shift, showing that the valence band maximum shifts from 2.94 to 3.31 eV upon doping with yttrium (Supplementary Fig. 33). As illustrated in Supplementary Fig. 34, electronic interactions can be perceived as a coupling between the valence states of the adsorbate and the *d* states the metal, giving

rise to bonding and antibonding states<sup>60</sup>. Of particular importance is the position of the antibonding state, intimately tied to the *d*-band center, which plays a pivotal role in governing the adsorption strength<sup>61,62</sup>. Yttrium doping instigates a downward shift of the *d*-band center and facilitates the formation of a low-energy antibonding state. Consequently, the diminished adsorption of H\* favors hydrogen production<sup>42</sup>. Overall, the lattice expansion induced by yttrium doping tunes the *d*-band center of the NiMo alloy, while the concurrently generated oxygen vacancies facilitate the electron transfer during HER.

The chemisorption models of intermediate species (e.g., H<sub>2</sub>O, activated H<sub>2</sub>O, \*OH, and H\*) on NiMo, Y-NiMo, MoO<sub>2</sub>, and MoO<sub>2-x</sub> surfaces are optimized, and the corresponding adsorption energies are evaluated by DFT calculations (Supplementary Fig. 35). Figure 4e presents the calculated kinetic energy barrier of water dissociation on NiMo, Y-NiMo, MoO<sub>2</sub>, and MoO<sub>2-x</sub>. The water dissociation barrier for NiMo alloy (0.62 eV) is lower than that of MoO<sub>2</sub> (0.94 eV), indicating NiMo sites are more conducive to complete water dissociation into H\* and \*OH. The introduction of yttrium further reduces the barrier to 0.4 eV, effectively expediting the sluggish Volmer step in alkaline media. Additionally, the free energy for H\* adsorption ( $\Delta G_{H^*}$ ) is another valid descriptor for evaluating electrocatalytic activity toward HER in alkaline media and allows determining the step of conversion of the as-formed H\* intermediates into H<sub>2</sub> product. The  $\Delta G_{H^*}$  for Y-NiMo is evaluated at -0.44 eV (Fig. 4f), which is much smaller than that of NiMo (-1.05 eV), indicating a more conducive surface for the desorption of the generated hydrogen species. The adsorption energies for H<sub>2</sub>O\*, H\* and \*OH on MoO<sub>2</sub> and MoO<sub>2-x</sub> are also compared (Supplementary Fig. 36). A high adsorption energy (-2.72 eV) is calculated for \*OH on the MoO<sub>2</sub> surface, which increases to -2.92 eV with the introduction of oxygen vacancies, suggesting that MoO<sub>2-x</sub> can effectively transfer \*OH to attenuate the blocking effect. Figure 4g summarizes the key factors contributing to the excellent catalytic activity and stability of the Y-NiMo/MoO<sub>2-x</sub> catalyst. First, yttrium doping promotes the uniform

and dense growth of nanorods on the Ni foam substrate, facilitating rapid mass transport and bubble release. Second, yttrium doping tunes the *d*-band center of the NiMo alloy, accelerating water dissociation and the subsequent evolution of H\* intermediates. Third, yttrium doping modulates the concentration of oxygen vacancies in MoO<sub>2</sub>, which not only improves efficient electron transfer during the HER process but also promotes \*OH desorption, thereby preventing blocking effects.

### Overall seawater splitting and AEM electrolyzer performance

Considering the notable HER performance of the Y-NiMo/MoO<sub>2-x</sub> electrode in the alkaline electrolyte, its potential application in seawater electrolysis is further evaluated. Seawater electrolysis is an attractive alternative due to the abundance of seawater as well as its high conductivity and salinity (~3.5 wt.%)<sup>25,26,63</sup>. Alkaline seawater is chosen as the electrolyte for its advantages over natural seawater in water electrolysis. Firstly, natural seawater contains high concentrations of hard cations (Ca<sup>2+</sup> and Mg<sup>2+</sup>) that can form precipitates on the catalyst surface and block the active sites. In an alkaline environment, these cations precipitate as Mg(OH)<sub>2</sub> and Ca(OH)<sub>2</sub>, which can be easily removed (Supplementary Fig. 37)<sup>64</sup>. Secondly, the chlorine evolution reaction in seawater is less favorable at high pH levels due to a higher theoretical overpotential, thereby minimizing the formation of chlorine and hypochlorite at the elevated current densities<sup>5,65</sup>. Here, simulated alkaline seawater (1 M KOH + 0.5 M NaCl) and natural alkaline seawater (1 M KOH + seawater) were chosen as electrolytes to evaluate the performance of the Y-NiMo/MoO<sub>2-x</sub> electrode in the presence of corrosive chloride ions as well as the complex ionic composition in natural seawater. Figure 5a compares the polarization curves of the Y-NiMo/MoO<sub>2-x</sub> electrode in alkaline water (1 M KOH), simulated alkaline seawater (1 M KOH + 0.5 M NaCl) and natural alkaline seawater (1 M KOH + seawater) media. Slight decreases in HER activity are noticed in the simulated and natural alkaline seawaters compared to those in the pure alkaline electrolyte, which can be ascribed to Cl<sup>-</sup> ions

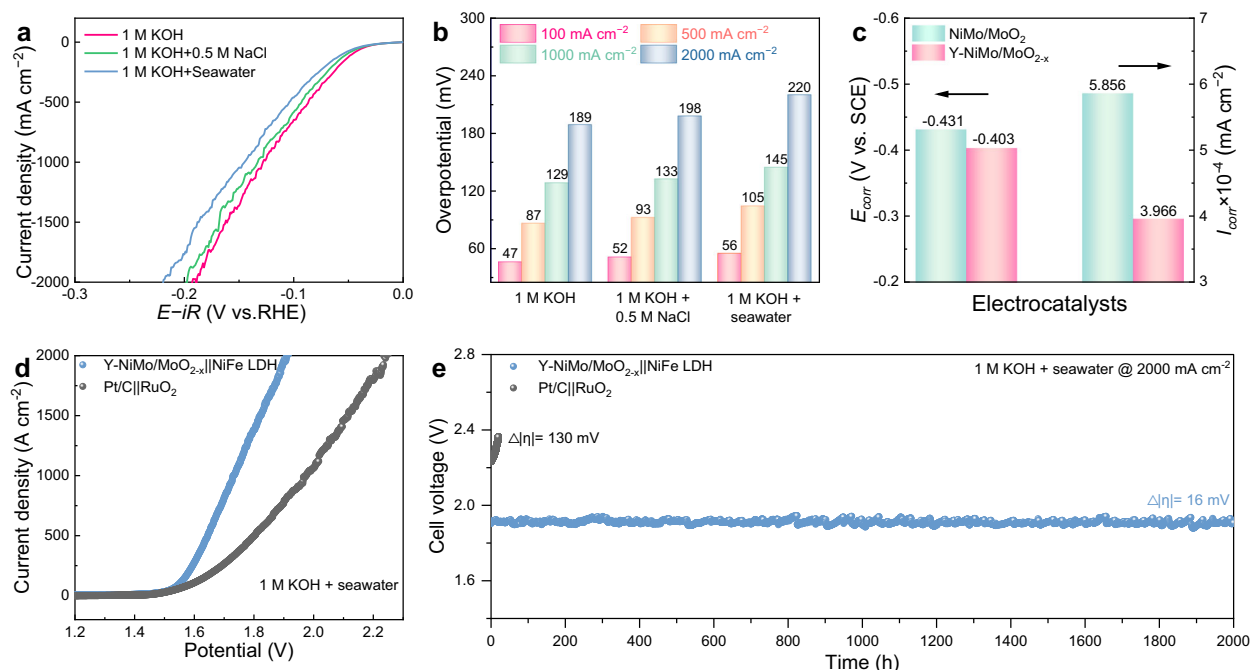


**Fig. 5 | Electrochemical hydrogen production performance.** **a** The polarization curves of Y-NiMo/MoO<sub>2-x</sub> electrode in 1 M KOH, 1 M KOH + 0.5 M NaCl, and 1 M KOH + seawater. **b** The comparison of overpotential required for Y-NiMo/MoO<sub>2-x</sub> at current densities up to 100, 500, 1000, and 2000 mA cm<sup>-2</sup> in different electrolytes. **c**  $E_{corr}$  and  $I_{corr}$  of NiMo/MoO<sub>2</sub> and Y-NiMo/MoO<sub>2-x</sub> catalysts in natural seawater.

**d** The polarization curves for overall water splitting of electrolyzer based on Y-NiMo/MoO<sub>2-x</sub>||NiFe LDH and Pt/C||RuO<sub>2</sub> couples in 1 M KOH + seawater. **e** The long-term stability test of Y-NiMo/MoO<sub>2-x</sub>||NiFe LDH and Pt/C||RuO<sub>2</sub> couples in 1 M KOH + seawater.

adsorbing on the electrode surface and reducing the interfacial charge transfer on the catalyst<sup>66</sup>. The overpotentials required for the Y-NiMo/MoO<sub>2-x</sub> electrode to deliver current densities of 100, 500, 1,000 and 2000 mA cm<sup>-2</sup> in the simulated alkaline seawater are 52, 93, 133, and 198 mV, respectively, which are almost identical to those obtained in alkaline water (Fig. 5b). The HER activity is even excellent in the complex natural alkaline seawater, and the Y-NiMo/MoO<sub>2-x</sub> electrode delivers current densities of 100, 500, 1000 and 2000 mA cm<sup>-2</sup> at considerably small overpotentials of 56, 105, 145 and 220 mV, respectively, which are remarkably lower than those obtained for the pristine NiMo/MoO<sub>2</sub> electrode (Supplementary Fig. 38). The achieved HER activity of the Y-NiMo/MoO<sub>2-x</sub> electrode in simulated and natural alkaline seawaters is compared with the recently reported electrocatalysts (Supplementary Table 13). The Y-NiMo/MoO<sub>2-x</sub> is currently positioned as one of the leading non-precious metal-based electrocatalysts for alkaline seawater electrolysis. Furthermore, the corrosion behavior of the electrodes during seawater electrolysis is investigated. Supplementary Fig. 39 presents the potentiodynamic polarization curves of NiMo/MoO<sub>2</sub> and Y-NiMo/MoO<sub>2-x</sub> electrodes under open circuit potential test conditions in natural alkaline seawater. Using Tafel extrapolation<sup>67</sup>, the corrosion current density of the Y-NiMo/MoO<sub>2-x</sub> electrode is determined to be merely  $3.966 \times 10^{-4}$  mA cm<sup>-2</sup>, which is lower than  $5.856 \times 10^{-4}$  mA cm<sup>-2</sup> for the NiMo/MoO<sub>2</sub> electrode (Fig. 5c). This suggests that yttrium doping enhances the corrosion resistance of the heterostructure electrode. Obtaining a higher corrosion potential for Y-NiMo/MoO<sub>2-x</sub> (-0.403 V) compared to NiMo/MoO<sub>2</sub> (-0.431 V) further signifies the increased resistance to corrosion in seawater.

A two-electrode configuration is constructed by employing Y-NiMo/MoO<sub>2-x</sub> as cathode and NiFe layered double hydroxides (LDHs) as anode to evaluate the overall water splitting performance in natural

alkaline seawater. For comparison, an electrolyzer made of commercially available precious metal catalysts with Pt/C as the cathode and RuO<sub>2</sub> as the anode is used. As shown in Fig. 5d, the voltages required for the Y-NiMo/MoO<sub>2-x</sub>||NiFe LDHs electrolyzer to deliver current densities of 100, 500, 1000, and 2000 mA cm<sup>-2</sup> are 1.55, 1.65, 1.73, and 1.91 V, respectively, much lower than those obtained for the Pt/C||RuO<sub>2</sub> electrolyzer (1.59, 1.80, 1.97, and 2.24 V, respectively). The durability of Y-NiMo/MoO<sub>2-x</sub>||NiFe LDHs and Pt/C||RuO<sub>2</sub> electrolyzers is also examined in natural alkaline seawater. The Y-NiMo/MoO<sub>2-x</sub>||NiFe LDHs electrolyzer exhibits comparable stability without noticeable degradation for over 2000 h at a high current density of 2 A cm<sup>-2</sup> (Fig. 5e). In contrast, the Pt/C||RuO<sub>2</sub> electrolyzer shows a voltage deviation of 130 mV after only 20 h of operation.

A natural alkaline seawater AEM electrolyzer is constructed with a membrane electrode assembly as illustrated in Fig. 6a to further evaluate the performance and durability of the Y-NiMo/MoO<sub>2-x</sub> heterostructure. The natural alkaline seawater AEM electrolyzer primarily comprises cathodic and anodic current collectors and gaskets, the cathode catalyst layer (Y-NiMo/MoO<sub>2-x</sub>), an anion exchange membrane (X37-50 Grade T), and the anode catalyst layer (NiFe-LDHs) (Fig. 6b and Supplementary Fig. 41). This setup facilitates examining the performance of the fabricated heterostructure electrocatalyst in a configuration similar to practical applications. In this regard, the scale-up of catalysts and electrodes, including large area size of 5 × 5 cm<sup>2</sup> and 30 × 16 cm<sup>2</sup>, is performed for the natural alkaline seawater AEM electrolyzer (Supplementary Figs. 42 and 43). Figure 6c illustrates the obtained *j*-V curves from the electrolyzer under varying electrolysis temperatures. The electrolyzer shows an exceptional water electrolysis performance, requiring merely 1.78 V and 2.05 V of cell voltage to attain current densities of 1 A cm<sup>-2</sup> and 2 A cm<sup>-2</sup> in natural alkaline seawater (3 M KOH + seawater) at 80 °C. This underscores the high

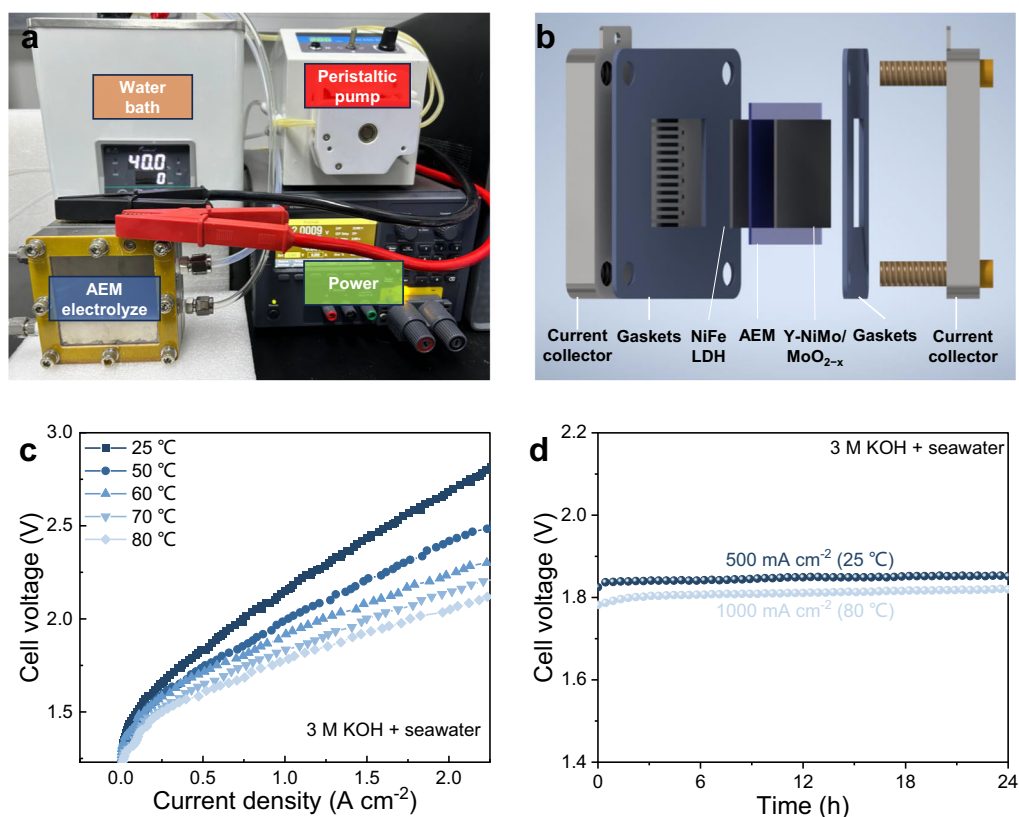


**Fig. 6 | Performance of electrolyzers.** **a** The photograph of a homemade natural alkaline seawater AEM electrolyzer and **b** the corresponding schematic diagram. **c** *j*-V curves of AEM electrolyzer loaded with Y-NiMo/MoO<sub>2-x</sub>||NiFe LDH operated at

different temperature in 3 M KOH + seawater. **d** The durability of electrolyzer measured at 500 mA cm<sup>-2</sup> (25 °C) and 1000 mA cm<sup>-2</sup> (80 °C) in 3 M KOH + seawater.

activity of the Y-NiMo/MoO<sub>2-x</sub> heterostructure catalyst even under stringent industrial conditions. The high activity also compares favorably to most previously reported non-precious metal-based electrocatalysts that were used in the AEM electrolyzer (Supplementary Table 14). Furthermore, the natural alkaline seawater AEM electrolyzer maintained stable operation for 24 h at a current density of 500 mA cm<sup>-2</sup> (25 °C) and 1000 mA cm<sup>-2</sup> (80 °C) (Fig. 6d), highlighting its robustness for industrial applications.

## Discussion

Optimization of water dissociation and adsorption/desorption of H\* and \*OH intermediates in alkaline HER is essential for the development of efficient and stable catalysts under high current density electrolysis conditions. In this study, a NiMo/MoO<sub>2-x</sub> heterostructure with yttrium doping is designed to achieve highly efficient and durable alkaline HER performance at high current densities. The introduced yttrium not only induces lattice expansion to promote water dissociation and the evolution of the H\* intermediate to H<sub>2</sub> but also enhances oxygen vacancy concentration in the MoO<sub>2</sub> component to expedite desorption of \*OH intermediate. The \*OH intermediates are promptly relocated to the MoO<sub>2-x</sub> component, whereas H\* intermediates proceed with hydrogen evolution over NiMo alloy surface. As a result, the accelerated water dissociation over NiMo alloy yields H\* and \*OH intermediates and the heterostructure with MoO<sub>2</sub> facilitates HER charge transfer. Thereby, the fabricated Y-NiMo/MoO<sub>2-x</sub> heterostructure can exhibit superior HER performance in both alkaline waters and seawaters under high current density conditions and opens up new opportunities for the development of efficient and stable electrocatalysts to meet future industrial demands.

## Methods

### Chemicals

Ammonium molybdate tetrahydrate ((NH<sub>4</sub>)<sub>6</sub>Mo<sub>7</sub>O<sub>24</sub>·4H<sub>2</sub>O, 99%), nickel nitrate (Ni(NO<sub>3</sub>)<sub>2</sub>·6H<sub>2</sub>O, 99%), and ruthenium dioxide (RuO<sub>2</sub>, 99.9%) were purchased from Shanghai Aladdin Biochemical Technology Co., Ltd. Yttrium nitrate (Y(NO<sub>3</sub>)<sub>3</sub>, 99.99%), potassium hydroxide (KOH, 95%), urea (CH<sub>4</sub>N<sub>2</sub>O, 99%), ammonium fluoride (NH<sub>4</sub>F, 99%), manganese nitrate (Mn(NO<sub>3</sub>)<sub>2</sub>·4H<sub>2</sub>O, 98%), and platinum on carbon (Pt/C, 20%) were purchased from Shanghai Macklin Biochemical Technology Co., Ltd. Ferric nitrate (Fe(NO<sub>3</sub>)<sub>3</sub>·9H<sub>2</sub>O) and cobalt nitrate (Co(NO<sub>3</sub>)<sub>2</sub>·6H<sub>2</sub>O), and yttrium nitrate (Y(NO<sub>3</sub>)<sub>3</sub>·6H<sub>2</sub>O, 99.99%) were purchased from Shanghai Titan Scientific Co., Ltd. Nickel foam (NF, 99.9%) was purchased from Quanzhou Yunzongcheng New Material Co., Ltd. Nafion 117 (5%) was purchased from Sigma-Aldrich. All chemicals are of analytical purity and used without further purification.

### Synthesis of Y-NiMoO<sub>4</sub> and Y-NiMo/MoO<sub>2-x</sub> catalysts

To prepare Y-NiMoO<sub>4</sub>, 0.6979 g Ni(NO<sub>3</sub>)<sub>2</sub>·6H<sub>2</sub>O and 0.7415 g (NH<sub>4</sub>)<sub>6</sub>Mo<sub>7</sub>O<sub>24</sub>·4H<sub>2</sub>O were dissolved in 60 mL of Milli-Q water and stirred until a homogeneous solution formed. Y(NO<sub>3</sub>)<sub>3</sub>·6H<sub>2</sub>O was then added in different molar ratios (0.5%, 1.0%, 2.0%, 4.0%, and 8.0% relative to Ni), and the corresponding samples were denoted as 0.5% Y-NiMoO<sub>4</sub>, 1.0% Y-NiMoO<sub>4</sub>, 2.0% Y-NiMoO<sub>4</sub>, 4.0% Y-NiMoO<sub>4</sub> and 8.0% Y-NiMoO<sub>4</sub>, respectively. The nickel foam (NF, 3 cm × 4 cm) was cleaned by sequential ultrasonic treatments in 3 M hydrochloric acid, Milli-Q water, and ethanol for 15 min each. Then, the precursor solution was transferred to 100 mL stainless-steel Teflon-lined autoclave with a piece of cleaned nickel foam for reaction at 150 °C for 6 h. The obtained catalyst was thoroughly washed with deionized water and ethanol and dried at 60 °C for 12 h. For the synthesis of Y-NiMo/MoO<sub>2-x</sub>, the Y-NiMoO<sub>4</sub> precursor was reduced by heating in a tube furnace under an Ar/H<sub>2</sub> atmosphere (V/V=90/10) with a ramp rate of 5 °C min<sup>-1</sup> and held at 500 °C for 2 h.

### Synthesis of Y-CoMo/MoO<sub>2-x</sub> and Y-MnMo/MoO<sub>2-x</sub> catalysts

For comparison, 2% Y-CoMoO<sub>4</sub> and 2% Y-MnMoO<sub>4</sub> were synthesized using a similar approach. Co(NO<sub>3</sub>)<sub>2</sub>·6H<sub>2</sub>O (0.6985 g) or Mn(NO<sub>3</sub>)<sub>2</sub>·4H<sub>2</sub>O (0.6024 g) were used instead of Ni(NO<sub>3</sub>)<sub>2</sub>·6H<sub>2</sub>O as metal precursors for the respective catalysts. The obtained precursors were washed, dried, and then annealed under the same hydrogen atmosphere conditions as described for Y-NiMo/MoO<sub>2-x</sub> to yield Y-CoMo/MoO<sub>2-x</sub> and Y-MnMo/MoO<sub>2-x</sub> catalysts.

### Synthesis of NiFe LDH catalyst

NiFe LDH was synthesized by dissolving 0.1454 g Ni(NO<sub>3</sub>)<sub>2</sub>·6H<sub>2</sub>O, 0.2020 g Fe(NO<sub>3</sub>)<sub>3</sub>·9H<sub>2</sub>O, 0.1389 g NH<sub>4</sub>F, and 0.9009 g CH<sub>4</sub>N<sub>2</sub>O in 50 mL Milli-Q water. A cleaned NF was immersed in the precursor solution and reacted at 90 °C for 4 h. The obtained NiFe LDH catalyst was thoroughly washed with deionized water and ethanol and dried at 60 °C for 12 h.

### Preparation of Pt/C and RuO<sub>2</sub> catalyst on NF

The Y-NiMo/MoO<sub>2-x</sub> was loaded onto NF at an approximate mass of -2.0 mg cm<sup>-2</sup> based on the weight increase after hydrothermal reaction. For comparison, a homogeneous suspension was prepared by dispersing 20 mg of commercial Pt/C catalyst in a mixture containing 90 μL of 5 wt% Nafion, 260 μL of ethanol, and 650 μL of Milli-Q water. A 100 μL aliquot of this slurry was then applied to clean NF and air-dried at room temperature. The commercial RuO<sub>2</sub> catalyst was loaded onto NF in the same method as the Pt/C catalyst.

### Characterization

The morphology and elemental distribution of the samples were examined using scanning electron microscopy (SEM, ZEISS Gemini-SEM 500) and transmission electron microscopy (TEM, JEOL-JEM 2100F) coupled with EDS. Crystal structure and phase composition were analyzed by X-ray diffraction (XRD, PANalytical X'pert PRO) with Cu Kα radiation (40 kV, 40 mA). Raman spectra were recorded on a Horiba iHR320 spectrometer using a 532 nm He-Ne laser as the excitation source. The chemical composition and surface electronic states were characterized by X-ray photoelectron spectroscopy (XPS, Thermo Scientific K-Alpha). EPR spectroscopy was performed on a Bruker A300 instrument at -150 °C to detect unpaired electrons and paramagnetic species. The wettability of the catalysts was evaluated through contact angle (CA) measurements using a Dataphysics OCA20 instrument. Seawater composition was determined via ion chromatography (IC, Thermo Scientific Dionex Aquion). Ultraviolet photoelectron spectroscopy (UPS, Shimadzu AXIS SUPRA+) was used to probe the valence band electronic structure of the materials. X-ray absorption fine structure (XAFS) measurements were carried out at the Shanghai Synchrotron Radiation Facility (beamline BL14W1, China) in transmission mode for the Ni and Mo K edges and in fluorescence mode for the Y K edge. Data preprocessing, including background subtraction, normalization, and Fourier transformation, was performed using the ATHENA software package (version 0.9.26)<sup>68</sup>. Wavelet transform analysis of the χ(k) data was conducted using the Hama Fortran code for advanced structural insights<sup>69</sup>.

### Electrochemical measurements

The electrochemical experiments were conducted using an Autolab (PGSTA302N) workstation equipped with a BOOSTER10A module in a three-electrode configuration. A three-electrode setup was employed, where the prepared catalyst (active area: 1 × 1 cm<sup>2</sup>) was used as the working electrode, a 3 mm diameter graphite rod as the counter electrode, and a Hg/HgO electrode as the reference electrode. This configuration was chosen for its compatibility with alkaline electrolytes and reliable signal stability. The electrolyte (1 M KOH) was prepared by dissolving 56.11 g of KOH in Milli-Q water to make up a total volume of 1000 mL, followed by storage in a PTFE

bottle to prevent contamination. The solution exhibited a pH of  $13.8 \pm 0.1$ . Calibration of the Hg/HgO reference electrode relative to the reversible hydrogen electrode (RHE) was performed in H<sub>2</sub>-saturated 1 M KOH solution. The potential was converted using the equation:  $E_{\text{RHE}} = E_{\text{Hg/HgO}} - E_{\text{offset}}^{70}$ . Here,  $E_{\text{offset}}$  was determined via cyclic voltammetry (CV) at a scan rate of  $1 \text{ mV s}^{-1}$  in the hydrogen electrocatalytic potential range, using a platinum foil electrode. The  $E_{\text{offset}}$  value was obtained as the average of the two zero-current intercepts on the CV curve. All polarization curves measurements were conducted after 30 CV conditioning cycles. The resulting polarization curves were  $iR$ -compensated (90%) to account for solution resistance. EIS data were collected across a frequency range from 0.1 to  $10^5$  Hz. For in situ EIS studies, potentials ranging from 0 to 1.0 V (vs. RHE) were applied under identical frequency conditions. The electrochemical double-layer capacitance ( $C_{\text{dl}}$ ) was determined via CV in a non-faradaic potential range (0.424–0.524 V vs. RHE) at scan rates of 20–100  $\text{mV s}^{-1}$ . The  $C_{\text{dl}}$  value was obtained from the slope of the linear fit between the current density difference ( $\Delta j$ ) and the scan rate using the relation:  $C_{\text{dl}} = d(\Delta j)/2dv$ . The electrochemically active surface area (ECSA) was then estimated as:  $\text{ECSA} = C_{\text{dl}} / C_s$ , where  $C_s$  was taken as  $11 \mu\text{F cm}^{-2}$ . The TOF was calculated to evaluate the intrinsic activity of the catalyst using the equation:  $\text{TOF} = j \times A / (4 \times F \times n)$ . Here,  $j$  is the current density,  $A$  is the electrode area,  $F$  is the Faraday constant, and  $n$  is the number of moles of active material. The  $n$  value was derived from the integrated charge ( $Q$ ) in cyclic voltammograms conducted in a 1 M PBS solution (pH = 7) at a scan rate of  $50 \text{ mV s}^{-1}$ :  $n = Q / (4 \times F)$ . Faradaic efficiency was quantified via gas-phase analysis during chronopotentiometric measurements conducted at a constant current density of  $10 \text{ mA cm}^{-2}$  in 1 M KOH. The TOF and Faradaic efficiency and TOF measurements were conducted once under controlled experimental conditions. Corrosion polarization curves were obtained in natural seawater to simulate practical conditions. Measurements employed a saturated glycolic electrode as the reference electrode, with the working electrode submerged for consistent exposure to the corrosive medium.

### AEM electrolyzer measurements

The AEM electrolyzer was assembled with an anode ( $5 \times 5 \text{ cm}$ ), cathode ( $5 \times 5 \text{ cm}$ ), and anion exchange membrane (AEM, X37-50 Grade T, Dioxide Materials). First, the AEM was immersed into 1 M KOH for 24 h before the construction of the AEM electrolyzer. The Y-NiMo/MoO<sub>2-x</sub> and NiFe LDH electrocatalyst with nickel foam was directly used as the cathode and anode, respectively, to construct the Y-NiMo/MoO<sub>2-x</sub>||NiFe LDH AEM electrolyzer. No additional processes, such as heating or pressing, are required for the assembly of AEM electrolyzer. Then the AEM electrolyzer was conducted at  $2 \text{ mA cm}^{-2}$  for 5 min to stabilize. The performance of AEM electrolyzer was investigated using a constant potentiostat (E36154A, Keysight) in natural alkaline seawater (3.0 M KOH + seawater) electrolyte at different temperatures (25–80 °C).

### DFT calculation

The Vienna Ab initio Simulation Package was used to conduct DFT calculations<sup>71</sup>. The exchange-correlation interactions were treated by applying the Perdew–Burke–Ernzerhof (PBE) functional within the generalized gradient approximation<sup>72</sup>. Projector augmented wave (PAW) pseudopotentials were utilized for ion-electron interactions, with a plane-wave cutoff energy of 500 eV<sup>73</sup>. Convergence criteria were set to  $10^{-5}$  eV for electronic energy and  $0.03 \text{ eV \AA}^{-1}$  for atomic forces. The catalytic surfaces of NiMo alloys, yttrium-doped NiMo alloys, MoO<sub>2</sub>, and MoO<sub>2-x</sub> with oxygen vacancies were modeled, and the adsorption of water (H<sub>2</sub>O) and intermediates (\*OH and \*H) was examined on various active sites of these materials. The adsorption geometries were optimized, and the DOS for each catalyst was

calculated to gain insights into the electronic structure, which is essential for understanding their catalytic properties. The adsorption energies of \*OH and \*H intermediates during the HER in an alkaline medium were calculated using the following thermodynamic expression:  $G = E_{\text{DFT}} + E_{\text{ZPE}} - T\Delta S$ , where  $E_{\text{DFT}}$  represents the DFT-calculated energy,  $E_{\text{ZPE}}$  is the zero-point energy obtained from vibrational analysis, and  $T\Delta S$  accounts for the entropy contribution. Thermodynamic corrections for the gas-phase molecules were obtained from standard reference databases.

### Data availability

The data supporting the findings of this study are available within the article and its Supplementary Information files. All other data are available from the corresponding author upon request. Source Data file has been deposited in Figshare under accession code <https://doi.org/10.6084/m9.figshare.27532875><sup>74</sup>.

### References

1. Yu, Z. et al. Clean and affordable hydrogen fuel from alkaline water splitting: past, recent progress, and future prospects. *Adv. Mater.* **33**, 2007100 (2021).
2. Zhu, J., Hu, L., Zhao, P., Lee, L. & Wong, K. Recent advances in electrocatalytic hydrogen evolution using nanoparticles. *Chem. Rev.* **120**, 851–918 (2020).
3. Anantharaj, S. et al. Strategies and perspectives to catch the missing pieces in energy-efficient hydrogen evolution reaction in alkaline media. *Angew. Chem. Int. Ed.* **60**, 18981–19006 (2021).
4. Jin, M. et al. Strategies for designing high-performance hydrogen evolution reaction electrocatalysts at large current densities above  $1000 \text{ mA cm}^{-2}$ . *ACS Nano* **16**, 11577–11597 (2022).
5. Zhao, T. et al. Cooperative boron and vanadium doping of nickel phosphides for hydrogen evolution in alkaline and anion exchange membrane water/seawater electrolyzers. *Small* **19**, 2208076 (2023).
6. Xiao, X. et al. In situ growth of Ru nanoparticles on (Fe,Ni)(OH)<sub>2</sub> to boost hydrogen evolution activity at high current density in alkaline media. *Small Methods* **4**, 1900796 (2020).
7. Mu, X. et al. Breaking the symmetry of single-atom catalysts enables an extremely low energy barrier and high stability for large-current-density water splitting. *Energy Environ. Sci.* **15**, 4048–4057 (2022).
8. Yao, R. et al. Stable hydrogen evolution reaction at high current densities via designing the Ni single atoms and Ru nanoparticles linked by carbon bridges. *Nat. Commun.* **15**, 2218 (2024).
9. Sheng, W., Gasteiger, H. & Shao-Horn, Y. Hydrogen oxidation and evolution reaction kinetics on platinum: acid vs alkaline electrolytes. *J. Electrochem. Soc.* **157**, B1529 (2010).
10. Strmcnik, D. et al. Improving the hydrogen oxidation reaction rate by promotion of hydroxyl adsorption. *Nat. Chem.* **5**, 300–306 (2013).
11. Lao, M. et al. From fundamentals and theories to heterostructured electrocatalyst design: An in-depth understanding of alkaline hydrogen evolution reaction. *Nano Energy* **98**, 107231 (2022).
12. Fajin, J., Cordeiro, M. & Gomes, J. Density functional theory study of the water dissociation on platinum surfaces: general trends. *J. Phys. Chem. A* **118**, 5832–5840 (2014).
13. Trasatti, S. Work function, electronegativity, and electrochemical behaviour of metals: III. Electrolytic hydrogen evolution in acid solutions. *J. Electroanal. Chem. Interfacial Electrochem.* **39**, 163–184 (1972).
14. Sabatier, P. Hydrogénations et déshydrogénations par catalyse. *Ber. Dtsch. Chem. Ges.* **44**, 1984–2001 (1911).
15. Wang, J. et al. Non-precious-metal catalysts for alkaline water electrolysis: operando characterizations, theoretical calculations, and recent advances. *Chem. Soc. Rev.* **49**, 9154–9196 (2020).

16. Wang, X. et al. Rationally modulating the functions of Ni<sub>3</sub>Sn<sub>2</sub>-NiSnO<sub>x</sub> nanocomposite electrocatalysts towards enhanced hydrogen evolution reaction. *Angew. Chem. Int. Ed.* **62**, e202301562 (2023).
17. Park, S., To, D. & Myung, N. A review of nickel-molybdenum based hydrogen evolution electrocatalysts from theory to experiment. *Appl. Catal. A* **651**, 119013 (2023).
18. Nairan, A. et al. NiMo solid solution nanowire array electrodes for highly efficient hydrogen evolution reaction. *Adv. Funct. Mater.* **29**, 1903747 (2019).
19. Song, J. et al. Phase-separated Mo-Ni alloy for hydrogen oxidation and evolution reactions with high activity and enhanced stability. *Adv. Energy Mater.* **11**, 2003511 (2021).
20. Zhang, J. et al. Efficient hydrogen production on MoNi<sub>4</sub> electrocatalysts with fast water dissociation kinetics. *Nat. Commun.* **8**, 15437 (2017).
21. Westsson, E., Picken, S. & Koper, G. The effect of lattice strain on catalytic activity. *Chem. Commun.* **55**, 1338–1341 (2019).
22. Sun, Y. et al. Strong electronic interaction in dual-cation-incorporated NiSe<sub>2</sub> nanosheets with lattice distortion for highly efficient overall water splitting. *Adv. Mater.* **30**, 1802121 (2018).
23. Zhao, S. et al. Spontaneous formation of asymmetric oxygen vacancies in transition-metal-doped CeO<sub>2</sub> nanorods with improved activity for carbonyl sulfide hydrolysis. *ACS Catal.* **10**, 11739–11750 (2020).
24. Xiao, Z. et al. Engineering oxygen vacancies and nickel dispersion on CeO<sub>2</sub> by Pr doping for highly stable ethanol steam reforming. *Appl. Catal. B* **258**, 117940 (2019).
25. Huang, C. et al. Functional bimetal Co-modification for boosting large-current-density seawater electrolysis by inhibiting adsorption of chloride ions. *Adv. Energy Mater.* **13**, 2301475 (2023).
26. Guo L. et al. Phosphorus defect mediated electron redistribution to boost anion exchange membrane-based alkaline seawater electrolysis. *Adv. Energy Mater.* **14**, 2400975 (2024).
27. Sun, J. et al. Joule heating synthesis of well lattice-matched Co<sub>2</sub>Mo<sub>3</sub>O<sub>8</sub>/MoO<sub>2</sub> heterointerfaces with greatly improved hydrogen evolution reaction in alkaline seawater electrolysis with 12.4% STH efficiency. *Appl. Catal. B* **338**, 123015 (2023).
28. Dastafkan, K., Shen, X., Hocking, R., Meyer, Q. & Zhao, C. Mono-metallic interphasic synergy via nano-hetero-interfacing for hydrogen evolution in alkaline electrolytes. *Nat. Commun.* **14**, 547 (2023).
29. Chen, Y. et al. Self-templated fabrication of MoNi<sub>4</sub>/MoO<sub>3-x</sub> nanorod arrays with dual active components for highly efficient hydrogen evolution. *Adv. Mater.* **29**, 1703311 (2017).
30. Wei, J. et al. High-efficient electrocatalyst of MoNi<sub>4</sub>@MoO<sub>3-x</sub> nanorod for hydrogen evolution reaction in alkaline solutions. *J. Alloys Compd* **876**, 160152 (2021).
31. Yang, F. et al. A durable and efficient electrocatalyst for saline water splitting with current density exceeding 2000 mA cm<sup>-2</sup>. *Adv. Funct. Mater.* **31**, 2010367 (2021).
32. Liu, S. et al. Promoting the hydrogen evolution reaction through oxygen vacancies and phase transformation engineering on layered double hydroxide nanosheets. *J. Mater. Chem. A* **8**, 2490–2497 (2020).
33. Dury, F., Gaigneaux, E. & Ruiz, P. The active role of CO<sub>2</sub> at low temperature in oxidation processes: the case of the oxidative dehydrogenation of propane on NiMoO<sub>4</sub> catalysts. *Appl. Catal. A* **242**, 187–203 (2003).
34. Wang, Y. et al. Vanadium-incorporated CoP<sub>2</sub> with lattice expansion for highly efficient acidic overall water splitting. *Angew. Chem. Int. Ed.* **61**, e202116233 (2022).
35. Wu, Z. et al. Conversion of catalytically inert 2D bismuth oxide nanosheets for effective electrochemical hydrogen evolution reaction catalysis via oxygen vacancy concentration modulation. *Nano-Micro Lett.* **14**, 90 (2022).
36. Lei, F. et al. Oxygen vacancies confined in ultrathin indium oxide porous sheets for promoted visible-light water splitting. *J. Am. Chem. Soc.* **136**, 6826–6829 (2014).
37. Kang, Y. et al. Quasi-2D AgRuO<sub>3</sub> oxide with facilely activated basal planes for efficient H<sub>2</sub> evolution. *Adv. Funct. Mater.* **34**, 2310674 (2024).
38. Jiang, F. et al. Insights into the influence of CeO<sub>2</sub> crystal facet on CO<sub>2</sub> hydrogenation to methanol over Pd/CeO<sub>2</sub> catalysts. *ACS Catal.* **10**, 11493–11509 (2020).
39. Yu, J. et al. Defect-rich NiCeO<sub>x</sub> electrocatalyst with ultrahigh stability and low overpotential for water oxidation. *ACS Catal.* **9**, 1605–1611 (2019).
40. Liang, W. et al. Oxygen-vacancy-rich MoO<sub>2</sub> supported nickel as electrocatalysts to promote alkaline hydrogen evolution and oxidation reactions. *Chem. Eng. J.* **464**, 142671 (2023).
41. Lu, B. et al. Structurally disordered phosphorus-doped Pt as a highly active electrocatalyst for an oxygen reduction reaction. *ACS Catal.* **11**, 355–363 (2021).
42. Wang, K. et al. Cu-doped heterointerfaced Ru/RuSe<sub>2</sub> nanosheets with optimized H and H<sub>2</sub>O adsorption boost hydrogen evolution catalysis. *Adv. Mater.* **35**, 2300980 (2023).
43. Kang, X. et al. A corrosion-resistant RuMoNi catalyst for efficient and long-lasting seawater oxidation and anion exchange membrane electrolyzer. *Nat. Commun.* **14**, 3607 (2023).
44. Chen, G. et al. Yttrium- and nitrogen-doped NiCo phosphide nanosheets for high-efficiency water electrolysis. *Carbon Energy* **6**, e522 (2024).
45. Wang, M. et al. Alloying nickel with molybdenum significantly accelerates alkaline hydrogen electrocatalysis. *Angew. Chem. Int. Ed.* **60**, 5771–5777 (2021).
46. Duan, Y. et al. Bimetallic nickel-molybdenum/tungsten nanoalloys for high-efficiency hydrogen oxidation catalysis in alkaline electrolytes. *Nat. Commun.* **11**, 4789 (2020).
47. Zhu, Y. et al. Facilitating alkaline hydrogen evolution reaction on the hetero-interfaced Ru/RuO<sub>2</sub> through Pt single atoms doping. *Nat. Commun.* **15**, 1447 (2024).
48. Zhang, R. et al. Single-atomic platinum on fullerene C<sub>60</sub> surfaces for accelerated alkaline hydrogen evolution. *Nat. Commun.* **14**, 2460 (2023).
49. Yu, L. et al. Non-noble metal-nitride based electrocatalysts for high-performance alkaline seawater electrolysis. *Nat. Commun.* **10**, 5106 (2019).
50. Jothi, V. et al. Corrosion and alloy engineering in rational design of high current density electrodes for efficient water splitting. *Adv. Energy Mater.* **10**, 1904020 (2020).
51. Jia, H. et al. Unravelling electrocatalytic concerted diatomic-ensembles over superior hydrogen-evolution array structured by NiMo/Mo<sub>2</sub>N heteronanojunctions. *Appl. Catal. B* **343**, 123362 (2024).
52. Du, W., Shi, Y., Zhou, W., Yu, Y. & Zhang, B. Unveiling the in situ dissolution and polymerization of Mo in Ni<sub>4</sub>Mo alloy for promoting the hydrogen evolution reaction. *Angew. Chem. Int. Ed.* **60**, 7051–7055 (2021).
53. Liu, X. et al. Lattice strain with stabilized oxygen vacancies boosts ceria for robust alkaline hydrogen evolution outperforming benchmark Pt. *Adv. Mater.* **36**, 2405970 (2024).
54. Doyle, R. & Lyons, M. Kinetics and mechanistic aspects of the oxygen evolution reaction at hydrous iron oxide films in base. *J. Electrochem. Soc.* **160**, H142 (2013).
55. Su, H. et al. In-situ spectroscopic observation of dynamic-coupling oxygen on atomically dispersed iridium electrocatalyst for acidic water oxidation. *Nat. Commun.* **12**, 6118 (2021).

56. Bertoluzzi, L., Lopez-Varo, P., Jiménez, Tejada, J. & Bisquert, J. Charge transfer processes at the semiconductor/electrolyte interface for solar fuel production: insight from impedance spectroscopy. *J. Mater. Chem. A* **4**, 2873–2879 (2016).
57. Zhang, B., Jiang, Z., Shang, X., Li, S. & Jiang, Z. Accelerated hydrogen evolution reaction in Ni<sub>3</sub>P/MoP<sub>2</sub>/MoO<sub>2</sub> tri-phase composites with rich crystalline interfaces and oxygen vacancies achieved by plasma assisted phosphorization. *J. Mater. Chem. A* **9**, 25934–25943 (2021).
58. Du, H. et al. Durable electrocatalytic reduction of nitrate to ammonia over defective pseudobrookite Fe<sub>2</sub>TiO<sub>5</sub> nanofibers with abundant oxygen vacancies. *Angew. Chem. Int. Ed.* **62**, e202215782 (2023).
59. Nørskov J., Studt F., Abild-Pedersen F., Bligaard T. Fundamental concepts in heterogeneous catalysis. in *Fundamental Concepts in Heterogeneous Catalysis* (Wiley, 2014).
60. Chen, Z. et al. Tailoring the d-Band centers enables Co<sub>4</sub>N nanosheets to be highly active for hydrogen evolution catalysis. *Angew. Chem. Int. Ed.* **57**, 5076–5080 (2018).
61. Santos, E. & Schmickler, W. d-Band catalysis in electrochemistry. *ChemPhysChem* **7**, 2282–2285 (2006).
62. Vojvodic, A. & Nørskov, J. Optimizing perovskites for the water-splitting reaction. *Science* **334**, 1355–1356 (2011).
63. Liu, S., Ren, S., Gao, R., Liu, X. & Wang, L. Atomically embedded Ag on transition metal hydroxides triggers the lattice oxygen towards sustained seawater electrolysis. *Nano Energy* **98**, 107212 (2022).
64. Jin, H. et al. Stable and highly efficient hydrogen evolution from seawater enabled by an unsaturated nickel surface nitride. *Adv. Mater.* **33**, 2007508 (2021).
65. Tong, W. et al. Electrolysis of low-grade and saline surface water. *Nat. Energy* **5**, 367–377 (2020).
66. Dresp, S., Dionigi, F., Klingenhof, M. & Strasser, P. Direct electrolytic splitting of seawater: opportunities and challenges. *ACS Energy Lett.* **4**, 933–942 (2019).
67. McCafferty, E. Validation of corrosion rates measured by the Tafel extrapolation method. *Corros. Sci.* **47**, 3202–3215 (2005).
68. Ravel, B. & Newville, M. ATHENA, ARTEMIS, HEPHAESTUS: data analysis for X-ray absorption spectroscopy using IFEFFIT. *J. Synchrotron Radiat.* **12**, 537–541 (2005).
69. Funke, H., Scheinost, A. & Chukalina, M. Wavelet analysis of extended x-ray absorption fine structure data. *Phys. Rev. B* **71**, 094110 (2005).
70. Liang, Y. et al. Co<sub>3</sub>O<sub>4</sub> nanocrystals on graphene as a synergistic catalyst for oxygen reduction reaction. *Nat. Mater.* **10**, 780–786 (2011).
71. Kresse, G. & Furthmüller, J. Efficiency of ab-initio total energy calculations for metals and semiconductors using a plane-wave basis set. *Comput. Mater. Sci.* **6**, 15–50 (1996).
72. Perdew, J. P., Burke, K. & Ernzerhof, M. Generalized gradient approximation made simple. *Phys. Rev. Lett.* **77**, 3865–3868 (1996).
73. Kresse, G. & Joubert, D. From ultrasoft pseudopotentials to the projector augmented-wave method. *Phys. Rev. B* **59**, 1758–1775 (1999).
74. Liu S., Zhang Z., Dastafkan K., Shen Y., Wang M. Yttrium-doped NiMo-MoO<sub>2</sub> heterostructure electrocatalysts for hydrogen production from alkaline seawater. figshare, <https://doi.org/10.6084/m9.figshare.27532875> (2024).

## Acknowledgements

The authors acknowledge support from the National Key Research and Development program of China (2022YFB3803600), National Natural Science Foundation of China (22372065), Hubei Provincial Key Research and Development Program (2023BAB113) and the Australian Research Council (IC200100023, DP220103294). We thank engineer Jun Su in the Center of Optoelectronic Micro&Nano Fabrication and Characterizing Facility, WNLO of HUST for the support in the SEM and TEM tests. We also thank the Analytical and Testing Center of HUST for assistance with the measurements.

## Author contributions

M.W. C.Z. and Y.S. directed the research project and supervised the experimental design. S.L. conceived the idea and performed most of the experiments. Z.Z. contributed to the first-principles calculation. S.L. and K.D. assisted in analyzing the data. S.L., K.D., Y.S., C.Z., and M.W. wrote the paper. All authors discussed the results and commented on the manuscript.

## Competing interests

The authors declare no competing interests.

## Additional information

**Supplementary information** The online version contains supplementary material available at <https://doi.org/10.1038/s41467-025-55856-4>.

**Correspondence** and requests for materials should be addressed to Yan Shen, Chuan Zhao or Mingkui Wang.

**Peer review information** *Nature Communications* thanks Jingwen Ma, Hiroshi Sakaguchi and the other anonymous reviewer(s) for their contribution to the peer review of this work. A peer review file is available.

**Reprints and permissions information** is available at <http://www.nature.com/reprints>

**Publisher's note** Springer Nature remains neutral with regard to jurisdictional claims in published maps and institutional affiliations.

**Open Access** This article is licensed under a Creative Commons Attribution-NonCommercial-NoDerivatives 4.0 International License, which permits any non-commercial use, sharing, distribution and reproduction in any medium or format, as long as you give appropriate credit to the original author(s) and the source, provide a link to the Creative Commons licence, and indicate if you modified the licensed material. You do not have permission under this licence to share adapted material derived from this article or parts of it. The images or other third party material in this article are included in the article's Creative Commons licence, unless indicated otherwise in a credit line to the material. If material is not included in the article's Creative Commons licence and your intended use is not permitted by statutory regulation or exceeds the permitted use, you will need to obtain permission directly from the copyright holder. To view a copy of this licence, visit <http://creativecommons.org/licenses/by-nc-nd/4.0/>.

© The Author(s) 2025